ELSEVIER

Composites: Part A 33 (2002) 1073–1081

composites
Part A: applied science and manufacturing

www.elsevier.com/locate/compositesa

Prediction of the yarn trajectories on complex braided preforms

J.F.A. Kessels, R. Akkerman*

Composites Group, Department of Mechanical Engineering, University of Twente, P.O. Box 217, NL-7500 AE Enschede, The Netherlands

Received 18 December 2000; revised 24 May 2002; accepted 26 June 2002

Abstract

Braiding can be used to manufacture preforms for resin transfer moulding (RTM). With braiding, many yarns are used, non-geodesic yarn paths are possible, and the interlaced structure of braids provides typical mechanical properties such as high impact strength. Previously, several models were developed to predict the fibre angles on simple, stationary braided preforms, but not for complex, non-axisymmetric preforms. This paper presents a fast and efficient model to predict the fibre angles on complex biaxially braided preforms. The model is verified with experiments on two mandrels and the experimental and numerical results show good agreement. © 2002 Elsevier Science Ltd. All rights reserved.

Keywords: B. Directional orientation; C. Numerical analysis; E. Braiding; A. and E. Preform

1. Introduction

Braiding is an ancient technique. It has been used for decorative purposes for many centuries. With its industrialisation it is now commonly used for manufacturing belts and ropes. Automated braiding is also a suitable process for manufacturing reproducible preforms for resin transfer moulding (RTM). The highly interlaced structure of braids makes it possible to cover components with sharp curvatures and non-circular cross-sections, varying along the length of the component. Furthermore, the interlaced nature of braids provides high levels of impact strength. Typical examples of these RTM components are propeller blades, trailing arms for a helicopter landing gear and automotive space frame components. So far, it was by no means trivial to predict the mechanical properties of an arbitrary braid reinforced product, firstly because the fibre directions could not be predicted in advance. Although different authors presented models for simple circular braiding [1–4], these models are not suitable for the preforms indicated, with a non-axisymmetric cross-section, varying along the length of the component. Here, we refer to these as 'complex shapes'. This paper presents a model for the prediction of the yarn trajectories on these braided complex shapes.

2. Process description

An illustration of a horn-gear braiding machine is given in Fig. 1. The mandrel, supported by a holder (not shown in the figure), is located between the spools. The mandrel moves with an axial velocity V. The yarns are driven by spools in the spool plane. One group of yarns, denoted as the warp yarns, moves clockwise while the weft yarns move counter-clockwise, both with an angular velocity of $\pm\omega$. As shown in Fig. 2, the spools are passed over and under each other in an alternating fashion. The two yarn groups interlock, forming a closed biaxial fabric on the mandrel. Optionally a third group of yarns can be inserted through the horn gears. These yarns will be deposited in parallel to the mandrel axis, providing extra stiffness and strength in the axial direction of the now triaxially braided preform.

A guide ring with radius R_g leads the yarns towards the mandrel. The yarns converge to the mandrel and touch the mandrel at a distance H from the guide ring. The point, where a yarn touches the mandrel is denoted as the fell point. In operation, the mandrel with its holder can be driven to the right and left alternately for both forward and reverse braiding, and the layer of braid formed previously is covered (or 'overbraided') by the newly formed one. This enables braiding multilayered products in one run.

3. Model assumptions

A mathematical model was developed to describe the

* Corresponding author. Tel.: +31-53-489-2566; fax: +31-53-489-3471.
E-mail address: r.akkerman@wb.utwente.nl (R. Akkerman).

PII: S1359-835X(02)00075-1

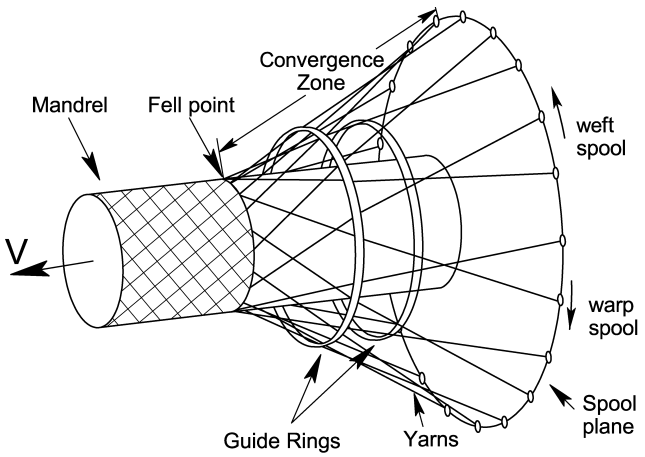

Fig. 1. Braiding machine.

braiding process and to predict the resulting fibre directions on a complex shape. This model is based on the following assumptions:

1. The yarn trajectories are continuous and differentiable.
2. The yarn trajectories have to lie on the mandrel surface.
3. After the yarns touch the mandrel, the relative motion between the yarns stops [2].
4. The yarns are straight in the convergence zone [3].

The first and second assumption sound trivial, but actually form the basis of the model. The first assumption implies that the yarn trajectories have certain smoothness without any kinks, while the second further restricts the spatial coordinates of the yarns. The third assumption is a stick condition. As in previous analyses, e.g. by Du and Popper [2], we assume that the yarn tension on the interlaced braided structure effectively locks the yarns on the mandrel surface, permitting non-geodesic yarn paths. Zhang et al. [3] analysed the effect of interyarn friction in the convergence zone. This friction leads to yarn curvature in the convergence zone and a certain decrease of the braid angle. These effects become more pronounced for an increasing number of spools. It can be shown that the fourth assumption is close to reality by elaborating this mechanics analysis for the braider, used in the experiments.

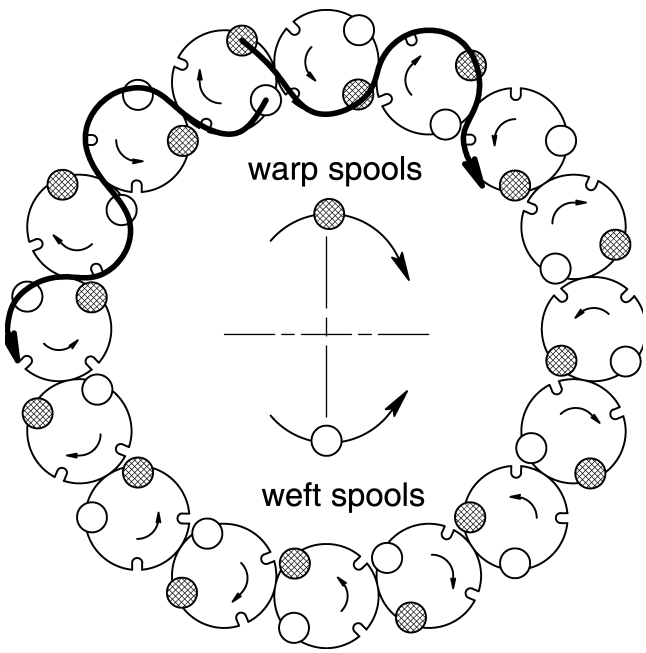

Fig. 2. Spool movement in the spool plane (with the thick arrows describing the actual paths).

4. Definitions

Fig. 3 shows a model of a braiding machine with a complex mandrel. Because it is assumed that the yarns are straight, and hence have no interaction, it is sufficient to describe one single yarn at a time. In this case, it can also be assumed that the spools rotate over the guide ring with radius R_g, instead of rotating on the spool plane. In Fig. 3, the position of the spool, $\vec{q}$, the surface of the mandrel, Q, and the fell point of the yarn, $\vec{p}$, can be seen. The angle between the path of the yarn and the tangent line of the surface in z-direction is the braid angle α.

The surface of the mandrel can be defined as a function Q for every point $\vec{x}$ on the surface:

$$Q(\vec{x}) = 0. \tag{1}$$

The path of the yarn on the mandrel, as shown in Fig. 3, can be defined as a trajectory $\vec{f}$. The fell point, $\vec{p}(t)$, moves along this trajectory in time. The fell point is therefore given by:

$$\vec{f}(\vec{p}(t)) = \vec{0}. \tag{2}$$

The coordinate system applied in Fig. 3 is fixed to the mandrel. Hence, the location of the fell point, $\vec{p}$, is invariant under displacement or rotation of the mandrel.

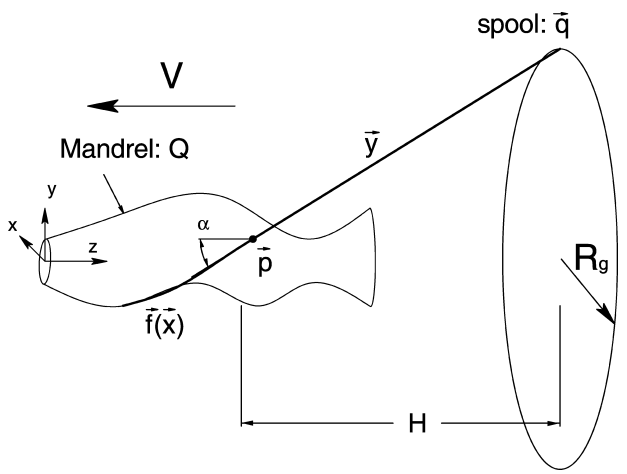

Fig. 3. Model of a braiding machine with a complex mandrel.

5. Mathematical relations

The four given assumptions form the basis of three mathematical relations. First of all, the yarn path has to be continuous and differentiable. This implies that the direction of the fibre path at the fell point, $\vec{p}$, has to be equal to the direction of the yarn path in the convergence zone:

$$\frac{\mathrm{d}}{\mathrm{d}t}\vec{p} = \lambda\cdot(\vec{p} - \vec{q}). \tag{3}$$

Secondly, the fibre path has to lie on the mandrel. This implies:

$$Q(\vec{p}) = 0. \tag{4}$$

At the fell point, the relative motion stops. Because the yarn trajectory is continuous, differentiable and lies on the mandrel surface, the yarn has to be tangential to the surface at the fell point. This can be written as:

$$(\vec{p} - \vec{q})\cdot\nabla Q(\vec{p}) = 0. \tag{5}$$

6. Numerical model

A numerical model was developed by discretising the mathematical relations (3)–(5). The equations are solved for discrete time steps, n. The position of the spool and the fell point at time step n, can be written as $\vec{q}_n$ and $\vec{p}_n$, respectively. In order to solve Eq. (5), the function $Q(\vec{p})$ is needed, which describes the mandrel surface in three-dimensional space. For most mandrels used in practice, the surface does not change dramatically in z-direction (the mandrel axis in Fig. 3) and therefore, Eqs. (4) and (5) can be approximated with:

$$Q\left(\begin{Bmatrix} p^x_{n+1} \\ p^y_{n+1} \\ p^z_n \end{Bmatrix}\right) = 0, \tag{6}$$

$$\left(\begin{Bmatrix} p^x_{n+1} \\ p^y_{n+1} \\ p^z_n \end{Bmatrix} - \begin{Bmatrix} q^x_{n+1} \\ q^y_{n+1} \\ q^z_n \end{Bmatrix}\right)\cdot\nabla Q\left(\begin{Bmatrix} p^x_{n+1} \\ p^y_{n+1} \\ p^z_n \end{Bmatrix}\right) = 0. \tag{7}$$

Instead of finding a tangent line on the mandrel surface in three-dimensional space it is now sufficient to find a tangent line on a curve in a plane with z-coordinate p^z_n. This significantly simplifies the calculations. Eqs. (6) and (7) provide a first estimation of the x- and y-coordinate of the next fell point (p^x_{n+1} and p^y_{n+1}). If a first-order Taylor series is used in Eq. (3), this leads to

$$\frac{\mathrm{d}}{\mathrm{d}t}\vec{p}_n \cong \frac{\vec{p}_{n+1} - \vec{p}_n}{\Delta t} = \lambda\cdot(\vec{p}_n - \vec{q}_n), \tag{8}$$

with λ as an arbitrary constant. Using the estimations of p^x_{n+1} and p^y_{n+1} in Eq. (8), the unknown variable λ can be found. With this variable known, Eq. (8) gives also an estimation of the new z-coordinate, p^z_{n+1}. At this z-coordinate Eqs. (6) and (7) can be solved again, giving a second approximation of the new x- and y-coordinates. This iteration process is continued until the differences between two subsequent approximations are smaller than the allowable tolerance, ε

$$\left|\vec{p}^{(i)}_{n+1} - \vec{p}^{(i-1)}_{n+1}\right| < \varepsilon. \tag{9}$$

7. Simulations and experiments

The presented model was implemented in the Matlab programming environment. A closed form solution of the braid angle, α^*, was given by Ko [1] for stationary braiding of axisymmetric preforms with a constant radius. It follows directly from the ratio of the tangential velocity and the axial velocity of the fell point and results in

$$\alpha^* = \arctan\left(\frac{P_\mathrm{m}\omega}{2\pi V}\right), \tag{10}$$

with P_m as the perimeter of the mandrel (equal to $2\pi R_\mathrm{m}$ for a circular cross-section of radius R_m). This expression (further indicated as the 'classical solution') was used to validate the discretisation of the numerical model for a circular cross-section, using a range of time step sizes. The input parameters are given in Table 1, where the convergence zone length, H, is the length with stationary braiding, given by Ref. [3]. The difference, E_2, between the closed form solution, α^*, and the results of the numerical model, using time step size Δt, is defined as

$$E_2(\Delta t) = \sqrt{\frac{\sum_{i=1}^{N}(\alpha^* - \alpha_i^{\Delta t})^2}{N}}, \tag{11}$$

with N as the number of time steps. Plotting this error function logarithmically against the time step size Δt leads to Fig. 4. The iterative scheme (further indicated as the 'three-dimensional numerical model') shows second-order convergence with decreasing step size.

The model was further validated on experimental data. A 96-spool braider of EuroCarbon in the Netherlands was used for these experiments. Two mandrels were designed for this purpose, as depicted in Fig. 5. The first mandrel has both a circular and square cross-section and was clamped eccentrically in the braiding machine, with an eccentricity of

Table 1
Parameters for the validation of the numerical model

Braiding parameter	Value
Initial convergence zone length, H	354.97 mm
Angular spool velocity, ω	6°/s
Mandrel velocity, V	5 mm/s
Mandrel radius, R_m	50 mm
Guide ring radius, R_g	375 mm
Closed form solution of the braid angle, α^*	46.32°

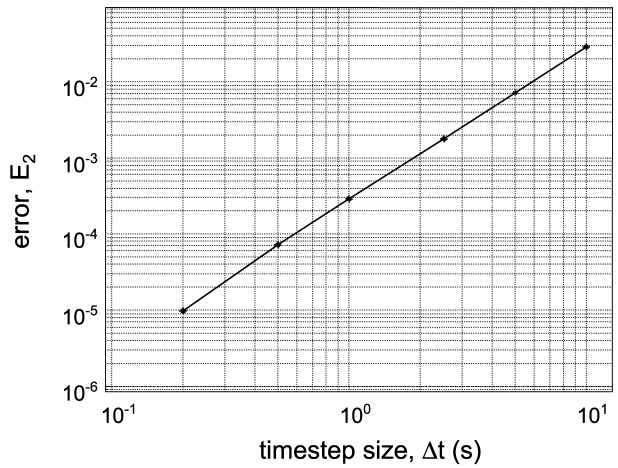

Fig. 4. Quadratic convergence of the three-dimensional numerical model with decreasing step size.

25 mm in the x-direction. As depicted in Fig. 6, the configuration is symmetric around the xz-plane, with the weft spools moving as the mirror image of the warp spools. Hence, the braid angles also show this symmetry, formally represented by

$$\alpha^{\text{warp}}(z,\beta) = -\alpha^{\text{weft}}(z,-\beta). \tag{12}$$

The second mandrel is more complicated. The cross-section of this mandrel changes its size and shape, and the mandrel has both centric and eccentric parts. Also for this mandrel the xz-plane is a plane of symmetry. The geometric details are given in Fig. 7. The corners of both mandrels were rounded off with a 15 mm radius.

The classical two-dimensional solution (Eq. (10)) can be extended to an approximation of the braid angle for an eccentric guide ring. A goniometric analysis with two coordinate systems, for the guide ring and the mandrel, respectively, as depicted in Fig. 8, leads to

$$\theta_1 = \arctan\left(\frac{R_0 \sin(\theta_0)}{R_0 \cos(\theta_0) + e}\right), \tag{13}$$

where (R_0, θ_0) are the polar coordinates of a point on the guide ring in the guide ring system, (R_1, θ_1) the polar

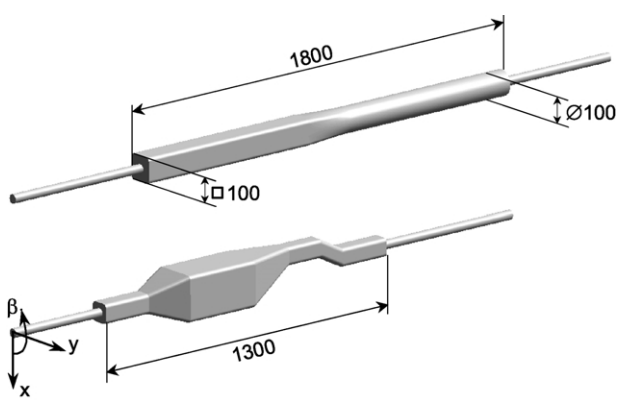

Fig. 5. Test mandrels 1 (top) and 2 (bottom), sizes in mm.

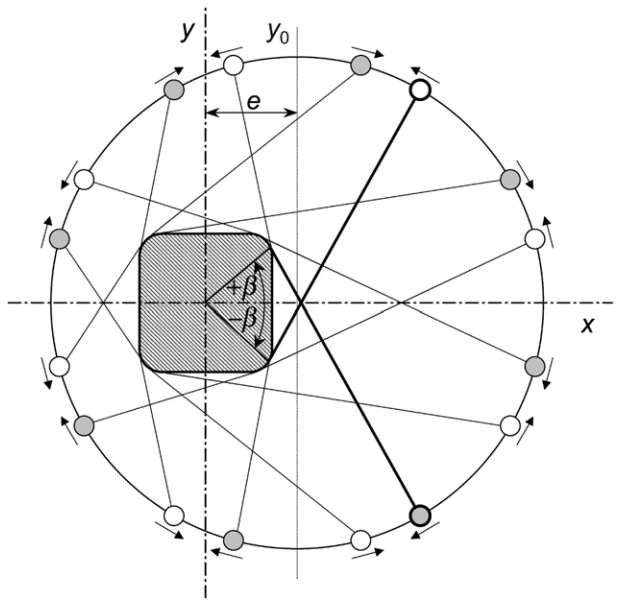

Fig. 6. Symmetry of the warp (grey) and weft (white) spools and yarns in the xz-plane for an eccentricity e in the x-direction.

coordinates of this point in the mandrel system and e is the eccentricity. The guide ring has a constant radius $R_0 = R_g$. The time derivative of this equation leads to a transformation of the angular velocity of a yarn on the guide ring

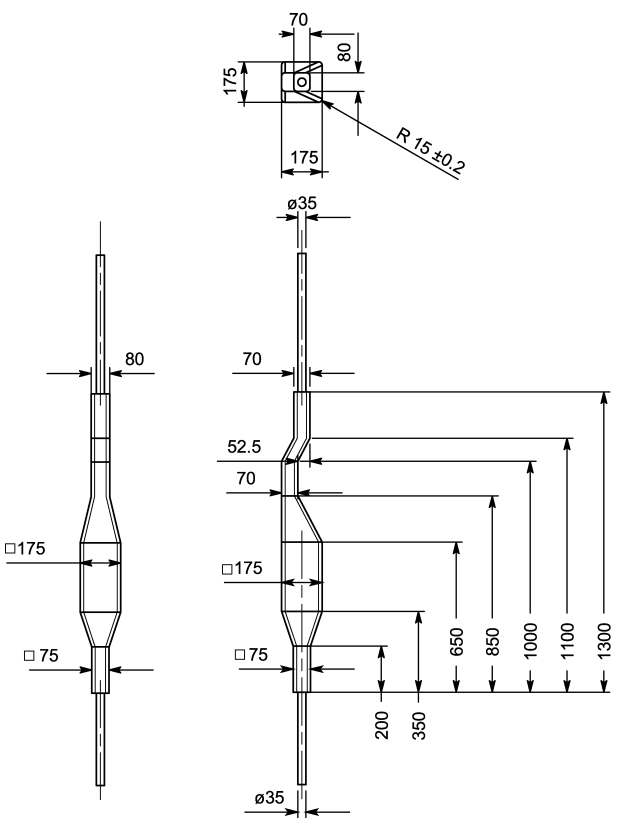

Fig. 7. Geometric details of mandrel 2 (sizes in mm).

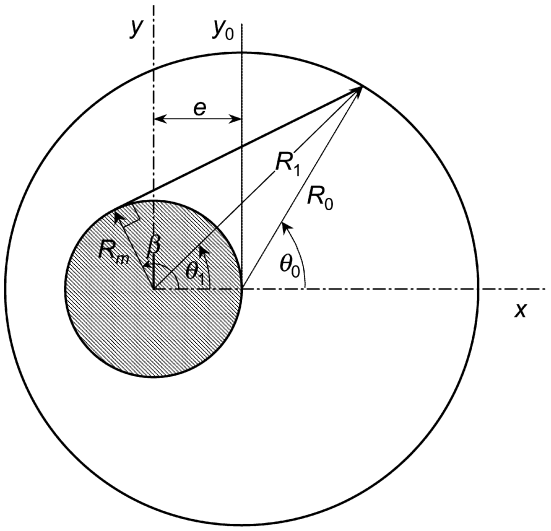

Fig. 8. Definition of the radii and angles in the guide ring coordinate system (R_0, θ_0) and the mandrel system (R_1, θ_1) for the two-dimensional model with eccentricity.

$\omega_0 (= \mathrm{d}\theta_0/\mathrm{d}t)$ in the guide ring system to the angular velocity ω_1 in the mandrel system:

$$\omega_1 = \omega_0 \frac{R_g(R_g + e\cos(\theta_0))}{R_g^2 + 2eR_g\cos(\theta_0) + e^2}. \quad (14)$$

Similar to Eq. (10), the braid angle can now be expressed as a function of the position of the yarn on the guide ring as

$$\alpha^*(\theta_0) = \arctan\left(\frac{P_m\omega_0}{2\pi V}\cdot\frac{R_g(R_g + e\cos(\theta_0))}{R_g^2 + 2eR_g\cos(\theta_0) + e^2}\right). \quad (15)$$

The closed form expression for the angle θ_0 in terms of the angle β of the fell point in the mandrel system is fairly complicated (Appendix A). However, a simple approximation can easily be established for an axisymmetric mandrel with a concentric guide ring

$$\theta_0 = \beta - \tfrac{1}{2}\pi + \arcsin\left(\frac{R_m}{R_g}\right), \quad (16)$$

in this case for the weft yarns (with the spools moving counter-clockwise). Combining Eqs. (15) and (16) gives a convenient closed form approximation (further indicated as the 'extended two-dimensional solution') of the braid angle along the circumference of the mandrel for the eccentric case.

Table 2
Braiding parameters for the test mandrels

Braiding parameter	Value for mandrel 1	Value for mandrel 2
Initial convergence zone length, $H_{initial}$ (mm)	200	160
Angular spool velocity, ω (°/s)	18	36
Mandrel velocity, V (mm/s)	26.3	16.67
Guide ring radius, R_g (mm)	170	170

The two mandrels were braided with the process parameters as given in Table 2. The braiding process was started around the supporting steel tube. The initial convergence length $H_{initial}$ was determined at the moment the braid reached the actual mandrel. The braider was mounted with 72 spools with glass yarns (tows of four 300 tex rovings of 13 μm EC glass from PPG, EC13.300.Z20.1383) and 24 spools with black polyester yarns (tows of four 110 tex rovings from Danfilex), thus obtaining good contrast for subsequent measurements. The braid angles were measured with a goniometer (with an accuracy of 20 min of angle) at nominally 25 mm intervals, along the four sides ($\beta = -90$, 0, 90, and 180°) of both mandrels.

8. Results

Fig. 9(a)–(d) presents the absolute braid angles on the first mandrel along the four sides, as found from the measurements, the classical solution (10), the extended two-dimensional solutions (15) and (16) and the three-dimensional numerical model. The 25 mm eccentricity leads to a distinct variation in braid angles. The braid angles of the warp and weft yarns are reasonably symmetric in the xz-plane. A 20% difference can be observed between the angles of the warp and weft yarns at $\beta = -90$ and 90° (with β as defined in Fig. 6), respectively. Notably, the difference is not largest between the two faces with the largest difference in distance to the guide ring.

The classical solution disregards the changes in both the tangential and axial velocity of the fell point. The tangential velocity is affected primarily by deviations from axisymmetry. This is included in the extended two-dimensional solution and leads to a significant improvement of the predictions. The axial velocity of the fell point is affected by the variation in the convergence zone length H. In practice, this is a very smooth variation, even when the mandrel cross-section changes abruptly. Only the three-dimensional numerical model captures this effect, leading to close approximations of the experimentally observed braid angles. The braiding process was started around the ∅35 mm steel tube supporting the mandrel. The abrupt change to the larger square cross-section initially leads to clustering of the yarns. This pattern gradually evolves into an even yarn distribution around the cross-section. As a consequence, the braid angles show strong fluctuations at the beginning of the mandrel, which are well captured in the numerical model. Also the gradual change of braid angle after the change of the mandrel cross-section (which can be attributed to the change in convergence zone length) is well predicted with the numerical model only.

All predictions for the first mandrel are combined in Fig. 10, which clearly illustrates the variation of the braid angle around the circumference and the location of the

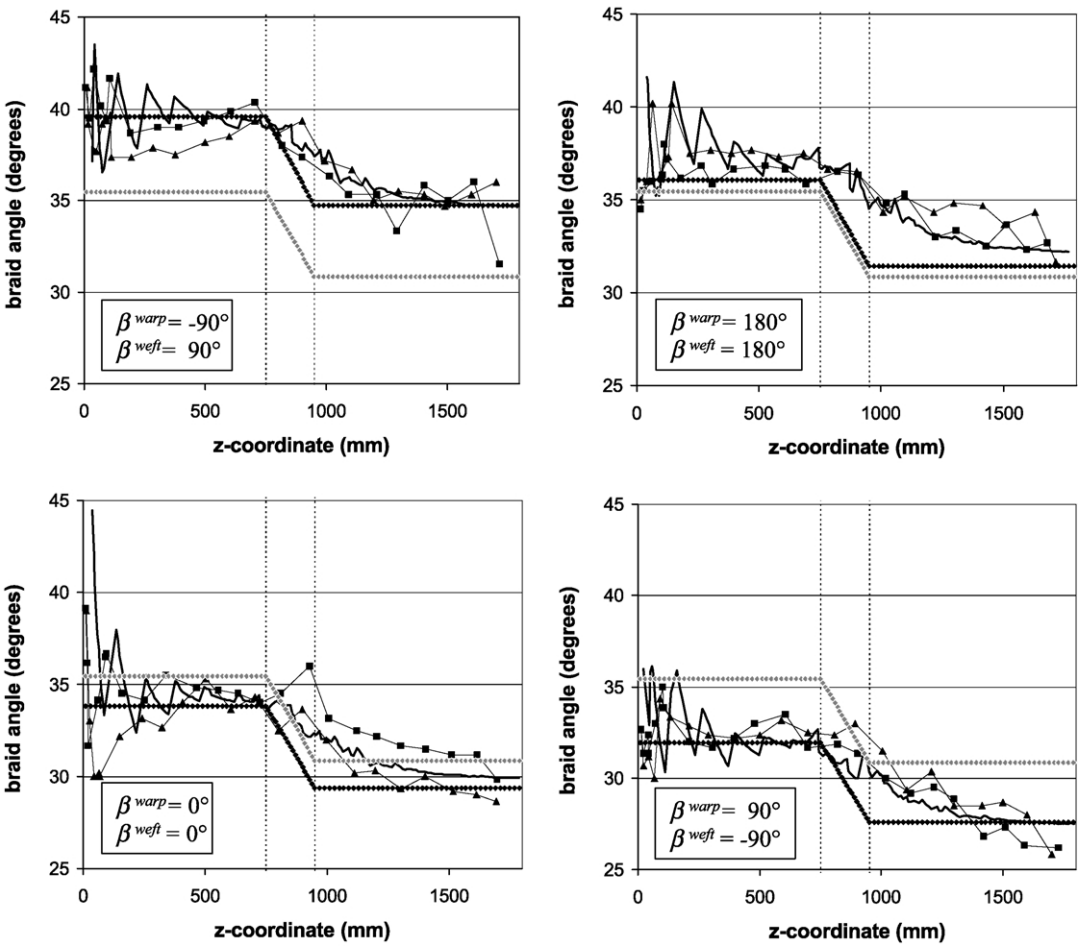

Fig. 9. Braid angles for mandrel 1. (◈) classical solution (10); (◆) extended two-dimensional solutions (15) and (16); (▲) experimental data warp yarns; (■) experimental data weft yarns; (▬) three-dimensional numerical solution.

extrema. It is clear from Fig. 8 that the fell point is approximately a quarter revolution ahead of the point of the warp yarn on the guide ring. The lowest relative angular velocity of the yarn (and correspondingly of the fell point) is found at the maximum yarn length between the mandrel and the guide ring. This maximum is found for $\theta_0 = 0°$ (Fig. 8), leading to the lowest angular velocity and the minimum braid angle for $\beta^{\text{warp}} = 90°$ in Fig. 10. The yarn length between the fell point and the guide ring decreases in the order $\beta^{\text{warp}} = 0$, 180, and $-90°$ and the braid angle can be seen to increase correspondingly.

The simulation results for the braid angles on the four faces of the second mandrel are presented in Fig. 11. Both the classical closed form solution (10) and the extended two-dimensional solutions (15) and (16) are included. In the first 650 mm the mandrel is concentric and all four predictions of the numerical model coincide, as well as all two-dimensional closed form solutions. Only after 500 mm the two- and three-dimensional predictions are approximately equal, indicating that the convergence zone length has adapted to the rapid changes in diameter and reaches its stationary value. After 650 mm the solutions for the four

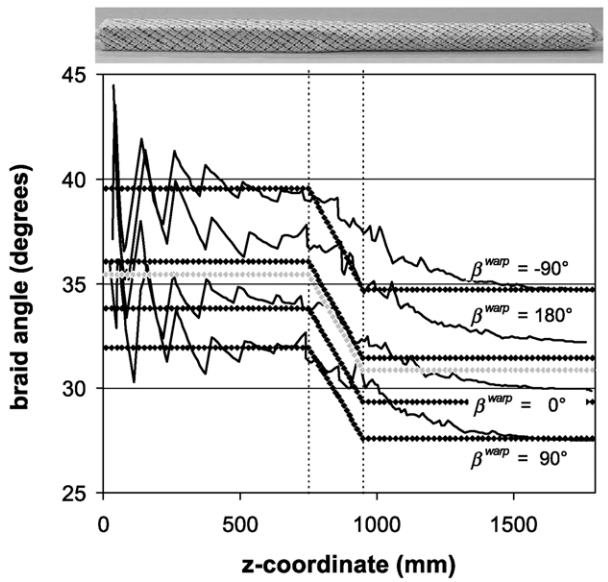

Fig. 10. Model results for the braid angles on mandrel 1 on four angles. (◈) classical solution (10); (◆) extended two-dimensional solutions (15) and (16); (▬) three-dimensional numerical solution.

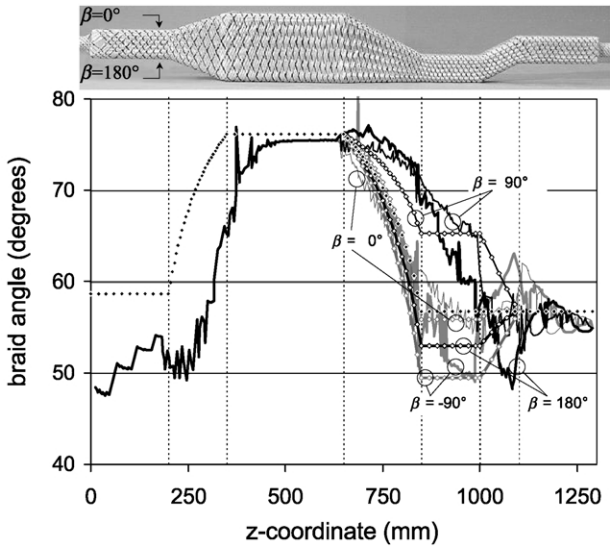

Fig. 11. Model results for the braid angles on mandrel 2 on four angles. (◆) classical solution (10); (–◇–) extended two-dimensional solutions (15) and (16); (▬) three-dimensional numerical solution.

faces diverge due to the eccentricity. As for the first mandrel, the braid angles at $\beta = 90$ and $-90°$ show the greatest difference. Apparently the convergence zone length closely follows its stationary value for $\beta = 0$ and $-90°$ in the convergent section between 650 and 850 mm, as the two- and three-dimensional results are very similar. On the other two faces these results differ considerably. When the yarns have approached a steady state braid angle, the eccentricity changes again between 1000 and 1100 mm, leading to further peaks in the braid angles. At the end of the final concentric section between 1100 and 1300 mm the four lines of the three-dimensional simulations are still not fully converged.

The experiments were performed with an increasing axial velocity. At the lowest velocity $V = 600$ mm/min it was observed that the yarns slipped over the conical part of the mandrel between 200 and 350 mm leading to 'yarn jamming', a loose wrinkled fabric resulting from sliding towards the smaller perimeter. Also in earlier experiments [5], slip was observed when braiding at a lower degree of coverage (less yarns per unit surface). In general, this slip is undesirable as it induces a largely uncontrolled fibre reorientation. It can be prevented by, e.g. using adhesive layers or, in this case, by braiding at a high degree of coverage, which is usually the case for preforms with high fibre contents. For $V = 1000$ mm/min this slip during braiding was no longer observed. No attempt was made to study the braiding process for higher axial velocities.

The experimentally obtained braid angles for these final process parameters (Table 2) are depicted in Fig. 12 for $\beta = 90$ and $-90°$ together with the various predictions. As was predicted by the three-dimensional simulations, the braid angles lag behind the changes in diameter for the first 500 mm. For $\beta^{warp} = -90°$ (the squares in Fig. 12) the simulation results follow the experimental values closely for the remainder of the mandrel. The experimental data for $\beta^{weft} = 90°$ (the triangles in Fig. 12) show a significant deviation from these values, not satisfying the symmetry condition (12). The cause of this deviation from symmetry of the warp and weft yarn paths is not confirmed yet; it is suspected that the weft yarns slipped over the mandrel after braiding. The results for $\beta^{warp} = 90°$ and $\beta^{weft} = -90°$ again satisfy the symmetry condition. Between 750 and 1100 mm the correlation with the three-dimensional simulation is not as good as before. Clearly the two-dimensionally predicted stepwise change of braid angle is not appropriate either. No definitive reason for this discrepancy can be given, based on the current records. The overall accuracy of the three-dimensional predictions is judged to be very acceptable, however.

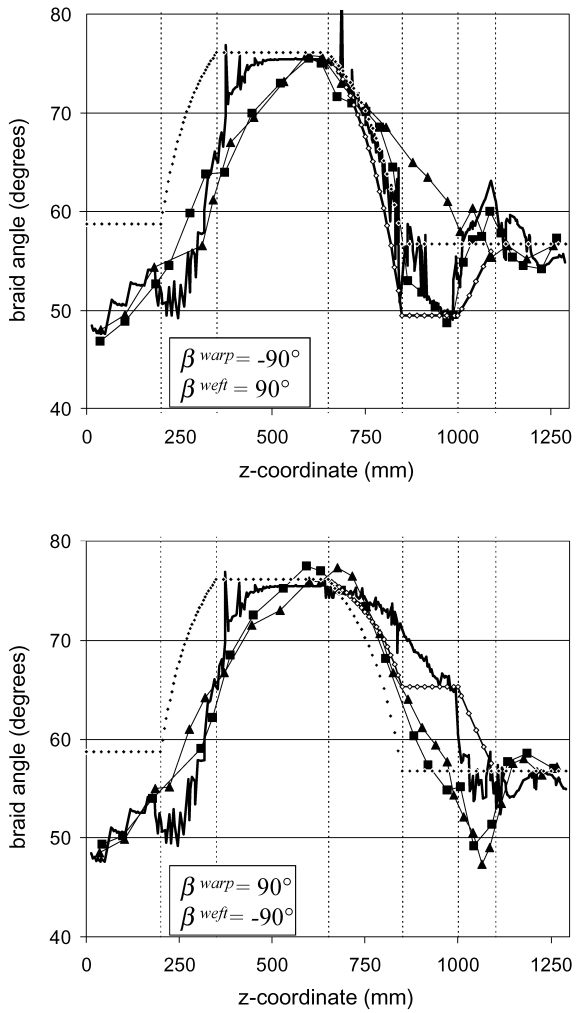

Fig. 12. Braid angles for mandrel 2. (◆) classical solution (10); (◇) extended two-dimensional solutions (15) and (16); (▲) experimental data warp yarns; (■) experimental data weft yarns; (▬) three-dimensional numerical solution.

9. Reflection

The novel three-dimensional model presented here predicts the yarn paths of biaxially braided composite components with the production parameters as input. This model is based on several assumptions. The first assumption is that the yarn trajectory has to be continuous and differentiable. Secondly the yarn paths have to lie on the mandrel. The yarns on both mandrels showed this behaviour. The third assumption, the stick condition on the mandrel, is true in general. However, especially in regions with a low degree of coverage (the percentage of yarn surface on the mandrel), the braid structure may be unable to lock all the yarns on the mandrel surface if it is sufficiently smooth. If, in this case, the yarns have to make a non-geodesic path, they start to slip after they are deposited. Usually, the braided preforms require high fibre contents, which prevent such a low degree of coverage. Due to the fourth assumption, the friction between the yarns in the convergence zone is neglected. During braiding, interyarn stick-slip friction was observed, but the experimental values of the braid angle are generally not below the simulated values as described in Ref. [3]. The model gives symmetric results for symmetric mandrels, also for offset cross-sections. The experimental results agree with this observation for the greater part, apart from the eccentric converging zone on the second mandrel. No definitive explanation can be given for this lack of symmetry in the experimental values. Further dedicated experiments should be performed to confirm our hypothesis of yarn slip after braiding. Further experiments are appropriate anyhow to enable a statistical analysis of the results.

Optimisation of biaxially braided composite components implies optimisation of the braid structure and hence of the fibre orientations. To accomplish this, the braiding process parameters must be determined from the desired product properties. This is a so-called inverse problem. The associated direct problem is to predict the braid structure of preforms from the braiding process parameters. Such a model was developed and presented in this paper. For simple circular braiding the inverse problem ('which machine settings are required to achieve the optimum fibre orientation?') is easily solved. In this case there is a direct relation (10) between the braid angle and the ratio of the axial and tangential velocities ([2]). It was shown for complex mandrels that the braid angle can no longer be expressed as a function of the current angular velocity ω and the axial velocity V only. The development of the braid angle along the component shows a certain path dependency, due to the variation in convergence zone length H. With the three-dimensional model, optimisation algorithms can be applied to solve this inverse problem for complex mandrels as well.

10. Conclusions

A first step in the optimisation of complex braided composite components is to predict the braid structure of preforms from the braiding process parameters. Such a model was developed and presented in this paper. The model is fast (calculation times are in the order minutes) and efficient (second-order convergence). The experimental results show good agreement with the predicted values, but further work is required to enable statistical analyses. Problems can occur when the braid structure has a low degree of coverage, due to which the yarns can slip after they are deposited. The current model is unable to predict these displacements. For the practical case of a usually high degree of coverage, the developed model gives a good prediction of the fibre directions in the braided composite, even if the product has non-circular cross-sections and sharp curvatures.

Acknowledgements

The support of EuroCarbon and the Dutch National Aerospace Laboratory NLR is gratefully acknowledged.

Appendix A. Two dimensional analysis of circular braiding with eccentricity

The yarn between the fell point and the guide ring can be described as a line $y = ax + b$. Considering Fig. 8, it has a slope

$$\frac{\mathrm{d}y}{\mathrm{d}x} = \tan(\beta - \tfrac{1}{2}\pi). \tag{A1}$$

A relation between β and θ_0 can be found by noting that both the fell point with (x, y) coordinates $(R_m \cos\beta, R_m \sin\beta)$ and the guide ring point $(e + R_g \cos\theta_0, R_m \sin\theta_0)$ are on this line. Solving this relation leads to

$$\theta_0 = \arctan\left(\frac{R_m - \sqrt{(R_g - R_m + e\cos^2\beta)(R_g + R_m - e\cos^2\beta)\sin^2\beta}\cos\beta - (R_m + e)\cos^2\beta + e\cos^4\beta}{(R_m\cos\beta + \sqrt{(R_g - R_m + e\cos^2\beta)(R_g + R_m - e\cos^2\beta)\sin^2\beta} - e\cos^3\beta)\sin\beta}\right), \tag{A2}$$

which can be shown to be approximated well by the linear relation in Eq. (16) which is more convenient for a first estimate of the braid angle.

References

[1] Ko FK. Braiding. Engineered materials handbook, volume 1, composites, ASM International; 1987. p. 519–28.
[2] Du GW, Popper P. Analysis of circular braiding process for complex shapes. J Text Inst 1994;85:316–37.
[3] Zhang Q, Beale D, Broughton RM. Analysis of circular braiding process. J Manufact Sci Engng 1999;121:345–50.
[4] Rosenbaum JA. Flechten, Rationelle Fertigung faserverstärkter Kunststofbauteile. Köln: Verlag TÜV Rheinland; 1991.
[5] Kessels JFA, Akkerman R. Simulations of the braiding process for RTM preforms. Proceedings of the Fifth International Conference on Textile Composites, Leuven; September 2000.